

# Interplay of Structural and Optoelectronic Properties in Formamidinium Mixed Tin–Lead Triiodide Perovskites

Elizabeth S. Parrott, Thomas Green, Rebecca L. Milot, Michael B. Johnston, Henry J. Snaith, and Laura M. Herz\*

Mixed lead–tin triiodide perovskites are promising absorber materials for low bandgap bottom cells in all-perovskite tandem photovoltaic devices. Key structural and electronic properties of the  $\text{FAPb}_{1-x}\text{Sn}_x\text{I}_3$  perovskite are presented here as a function of lead:tin content across the alloy series. Temperature-dependent photoluminescence and optical absorption measurements are used to identify changes in the bandgap and phase transition temperature. The large bandgap bowing parameter, a crucial element for the attainment of low bandgaps in this system, is shown to depend on the structural phase, reaching a value of 0.84 eV in the low-temperature phase and 0.73 eV at room temperature. The parabolic nature of the bowing at all temperatures is compatible with a mechanism arising from bond bending to accommodate the random placement of unevenly sized lead and tin ions. Charge-carrier recombination dynamics are shown to fall into two regimes. Tin-rich compositions exhibit fast, monoexponential recombination that is almost temperature-independent, in accordance with high levels of electrical doping. Lead-rich compositions show slower, stretched-exponential charge-carrier recombination that is strongly temperature-dependent, in accordance with a multiphonon assisted process. These results highlight the importance of structure and composition for control of bandgap bowing and charge-carrier recombination mechanisms in low bandgap absorbers for all-perovskite tandem solar cells.

efficiency<sup>[5]</sup> of 18.5%. These achievements have been enabled by the widely tuneable bandgap of mixed perovskites extending from 1.2 to 3.0 eV through alloying of the metal cation ( $\text{Pb}^{2+}$ ,  $\text{Sn}^{2+}$ ),<sup>[6,7]</sup> A-cation ( $\text{HC}(\text{NH}_2)_2^+$  (FA),  $\text{CH}_3\text{NH}_3^+$  (MA),  $\text{Cs}^+$ ),<sup>[8–10]</sup> and halide ( $\text{I}^-$ ,  $\text{Br}^-$ ,  $\text{Cl}^-$ ).<sup>[10–14]</sup> The benefit of tandem or multijunction solar cells is that they employ two or more semiconducting materials absorbing different portions of the solar spectrum, thus reducing charge thermalization losses and enabling a higher PCE than is possible for a single-junction cell.<sup>[15]</sup> Since a significant proportion of the overall cost of solar panels is made up of installation, structural, and land costs, all of which scale with area, high efficiency solar cells are important in reducing the resultant price of electricity.<sup>[16]</sup> However, tandem cells are typically expensive to make, offsetting the benefit of their higher efficiencies to energy prices,<sup>[17]</sup> and limiting their application. A perovskite tandem solar cell which retains the low-cost production of solution-processable materials while achieving the efficiency boost enabled by

multiple layers therefore has great potential to deliver large scale and affordable renewable energy.<sup>[18]</sup>

To achieve the highest efficiencies, tandem solar cells require a narrow bandgap semiconductor of around 0.8–1.2 eV to absorb the infrared portion of the solar spectrum.<sup>[18]</sup> To obtain such a low bandgap from a metal halide perovskite, one may utilize the interesting phenomenon of bandgap bowing observed when lead and tin perovskites are alloyed.<sup>[6]</sup> In contrast to the linear change in bandgap observed for metal halide perovskites with compositional changes in A-cation<sup>[8]</sup> and halide anion,<sup>[12]</sup> alloyed lead–tin perovskites have been found to exhibit lower bandgaps than either of the “parent” compositions  $\text{APbX}_3$  or  $\text{ASnX}_3$ . It is common for semiconductor alloys to display some degree of bandgap bowing, with the bandgap bowing parameter  $b$  being defined by the following equation<sup>[19]</sup>


$$E(x) = E_1x + E_2(1-x) + bx(1-x) \quad (1)$$

where  $E(x)$  is the bandgap energy of the mixed composition comprising material 1 with bandgap energy  $E_1$  and material 2

## 1. Introduction

Metal-halide perovskites ( $\text{ABX}_3$ ) are a type of solution processable yet highly crystalline semiconductor with high charge-carrier mobilities<sup>[1]</sup> and a direct optical bandgap,<sup>[2]</sup> showing promise for applications in solar cells with record power conversion efficiencies (PCEs) currently nearing that of crystalline silicon.<sup>[3]</sup> In addition to single-junction solar cells, all-perovskite tandem cells have been developed with a record four-terminal efficiency<sup>[4]</sup> of 23% and two-terminal

E. S. Parrott, T. Green, Dr. R. L. Milot, Prof. M. B. Johnston, Prof. H. J. Snaith, Prof. L. M. Herz  
Department of Physics  
University of Oxford  
Clarendon Laboratory, Parks Road, Oxford OX1 3PU, UK  
E-mail: laura.herz@physics.ox.ac.uk

 The ORCID identification number(s) for the author(s) of this article can be found under <https://doi.org/10.1002/adfm.201802803>.

DOI: 10.1002/adfm.201802803

with bandgap energy  $E_2$ , and  $x$  is the proportion of material 1. The first two terms represent a linear change in bandgap with composition between the two end points, and the third term captures a quadratic deviation from linearity. Equation (1) shows that a maximum deviation  $\Delta E$  occurs at  $x = 0.5$  and is given by  $\Delta E = b/4$  (see Figure 2a).

There is little understanding of the cause of bandgap bowing in metal halide perovskites at the present time, and reports disagree on both the origin<sup>[7,20]</sup> and magnitude of the effect. Hao,<sup>[6]</sup> Zhao,<sup>[21]</sup> Anaya,<sup>[22]</sup> and Liu<sup>[23]</sup> all report bowing in MAPb<sub>1-x</sub>Sn<sub>x</sub>I<sub>3</sub> with a minimum bandgap of just below 1.2 eV at around 80% tin fraction, determined from optical absorbance or external quantum efficiency (EQE) measurements. Yang<sup>[24]</sup> reports a minimum of 1.27 eV at 75% tin, Im<sup>[20]</sup> and Stoumpos<sup>[25]</sup> find a minimum bandgap of 1.1 eV at around 50% tin content, while Ogami finds the minimum bandgap to be 1.1 eV at 100% tin with little bowing. For FAPb<sub>1-x</sub>Sn<sub>x</sub>I<sub>3</sub>, Eperon<sup>[7]</sup> and Prasanna<sup>[9]</sup> report a minimum bandgap of 1.2 and 1.25 eV respectively at around 60% tin content. Clearly if these materials are to be optimized for tandem devices, a greater understanding and control of the factors influencing the bandgap are required.

Aside from the bandgap, other properties of the mixed perovskites are important in determining how the material will perform in a photovoltaic (PV) cell, namely the charge-carrier lifetimes and PL quantum efficiencies. Lifetimes must be sufficiently long for carriers to be extracted before they recombine, and nonradiative recombination pathways must be minimized to reach maximum efficiencies. All-perovskite tandem solar cells are limited in part by the poorer performance of perovskite materials containing tin.<sup>[7]</sup> For MASnI<sub>3</sub>, poor device performance has been linked to very fast charge-carrier recombination, largely as a result of spontaneous p-doping due to the formation of defects such as tin vacancies.<sup>[26–28]</sup> However the presence of spontaneous doping in mixed metal perovskites is less clear as there are only a handful of reports of charge recombination lifetimes for mixed metal perovskites in the literature to date. (FASn)<sub>0.6</sub>(MAPb)<sub>0.4</sub>I<sub>3</sub> is shown to have a PL lifetime intermediate to that of FASnI<sub>3</sub> and MAPbI<sub>3</sub>.<sup>[29]</sup> From optical pump terahertz probe spectroscopy the monomolecular and bimolecular recombination rates for FASn<sub>0.5</sub>Pb<sub>0.5</sub>I<sub>3</sub> also take intermediate values compared to values for 100% Sn or Pb reported elsewhere in the literature.<sup>[7]</sup> Zhao et al. show that metal composition has an impact on charge recombination mechanisms in MAPb<sub>1-x</sub>Sn<sub>x</sub>I<sub>3</sub>, with 20–40% Sn having much weaker photoluminescence than other compositions, and all tin-rich compositions having short PL lifetimes.<sup>[21]</sup> They show that the dominant recombination mechanism at low intensity is Shockley–Read–Hall (SRH) recombination, but that at high intensity, the 60% Sn composition, which gives highest device efficiency, becomes dominated by radiative recombination (as determined from the diode ideality factor).<sup>[21]</sup> To reduce SRH recombination, a defect passivating electron transport layer can be used, which has been shown to increase device efficiency for MASn<sub>0.5</sub>Pb<sub>0.5</sub>I<sub>3</sub>.<sup>[5]</sup> Finally, increasing film crystallinity and thickness is reported to increase the lifetime by an order of magnitude.<sup>[4]</sup> The charge-carrier lifetimes and recombination mechanisms of FAPb<sub>1-x</sub>Sn<sub>x</sub>I<sub>3</sub> have not yet been systematically studied as a function of metal composition, although FA has been shown to be a good choice of cation in mixed tin-

lead perovskites, improving stability<sup>[24]</sup> and PL lifetime,<sup>[30]</sup> and supporting single-junction PV devices that currently achieve PCEs of around 15%.<sup>[7,29]</sup>

In response to the broad lack of knowledge regarding these device-relevant materials, we investigate the optoelectronic properties of FAPb<sub>1-x</sub>Sn<sub>x</sub>I<sub>3</sub>, through photoluminescence and optical absorption measurements across the Pb-Sn spectrum at temperatures from 5 to 300 K. We highlight several key properties important for the improvement of mixed-metal halide perovskites and provide fundamental insights, through experiment and by drawing on the wealth of literature on traditional inorganic semiconductors. We report the structural phase transition temperatures as a function of composition, and show that the phase influences the magnitude of the bowing parameter and the gradient of the bandgap with temperature. We show that the charge-carrier recombination dynamics can be split into two regimes—fast, monoexponential recombination with a higher proportion of radiative recombination for tin-rich compositions and slower, stretched-exponential recombination for the lead-rich compositions. We also demonstrate that the charge recombination rate is almost temperature-independent for FASnI<sub>3</sub>, whereas there is strongly temperature activated nonradiative recombination in FAPb<sub>0.75</sub>Sn<sub>0.25</sub>I<sub>3</sub>, which we attribute to multiphonon assisted charge-carrier recombination.

## 2. Results and Discussion

### 2.1. Temperature-Dependence of the Bandgap

We first explore the general behavior of the bandgap with temperature, for several compositions with varying tin content. We observed discontinuities in the PL and absorption edge for all compositions which we ascribe to phase transitions, similar to what has been seen in other hybrid perovskite materials.<sup>[31,32]</sup> Figure 1a,b highlights this discontinuity for the 45% Sn ( $x = 0.45$ ) composition on color maps of the PL and the reflection-corrected absorption spectrum respectively, at temperatures between 5 and 295 K (see Figure S1 in the Supporting Information for color maps for different compositions). Figure 1c shows how the phase transition temperature changes with composition. The transitions of the end compositions agree with those reported in the literature, from PL<sup>[32]</sup> and X-ray diffraction<sup>[33]</sup> measurements for 100% lead and resistivity measurements for 100% tin.<sup>[34]</sup> Our results show that the transition temperature changes linearly with tin fraction between these end points. Further to the transitions in Figure 1c, we see a second discontinuity, only in FASnI<sub>3</sub>, which may indicate a further phase transition at 170 K. This could correspond to the Pnma (orthorhombic) to P4/mbm (tetragonal) transition reported at around 150 K by Schueller et al.<sup>[35]</sup> Schueller also reports a transition to a cubic structure at 250 K which from our results appears to have no influence on the PL. Comparing the other transitions with those reported in literature, FAPbI<sub>3</sub> is thought to be in a trigonal space group at low temperature, with a gentle transition to another trigonal space group, beginning at 100 K and completing at 175 K on heating,<sup>[32,33]</sup> which is in accordance with our results. Across the compositions at room temperature there is thought to be a structural change from

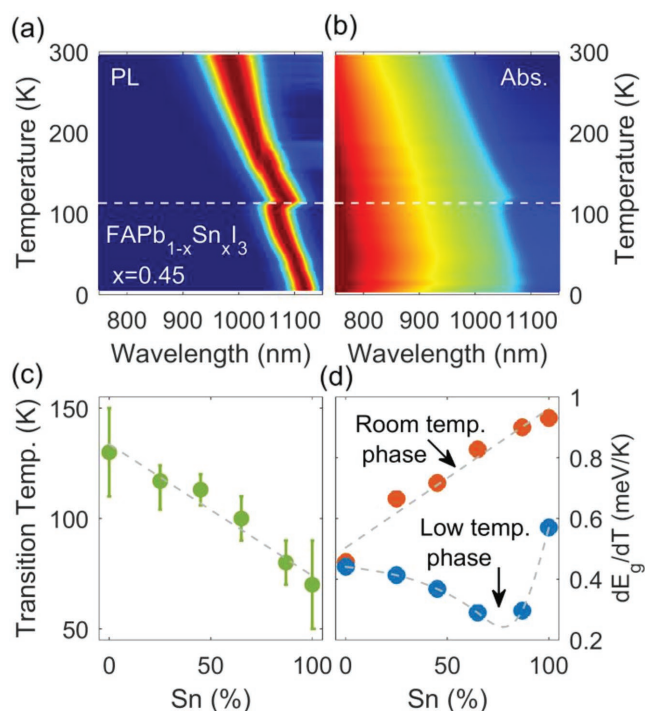


**Figure 1.** Example of a color map of a) PL intensity (sample excited at 400 nm,  $1 \text{ W cm}^{-2}$ ) and b) absorption coefficient of  $\text{FAPb}_{1-x}\text{Sn}_x\text{I}_3$ , showing spectra taken at different temperatures with intervals of 5 K. The identified phase transition is shown by the dashed white line. c) Lowest temperature phase transition for each tin composition, found from the discontinuity in PL and absorption edge energies when heating the sample from 4 K to room temperature. The error bars indicate the temperature range over which the discontinuity is found. d) Gradient of the absorption edge with respect to temperature for each composition in its room temperature phase and lowest temperature phase.

the space group  $P3m1$  (trigonal) for lead rich compositions to  $\text{Amm}2$  (orthorhombic) for tin rich compositions,<sup>[36,37]</sup> in the region of 25% tin.<sup>[7]</sup> However, in other studies  $\text{FASnI}_3$  has been reported to have cubic structure ( $\text{Pm}\bar{3}\text{m}$ ) at room temperature,<sup>[35]</sup> including in single crystals.<sup>[34,38]</sup>

Apart from the discontinuities at the phase transitions, the bandgap changes linearly with temperature. For all compositions, we observed that both the PL maximum and absorption onset blueshift as the temperature is increased, implying an increasing bandgap, as has been observed for all other metal halide perovskite semiconductors.<sup>[26,31,39,40]</sup> This finding is contrary to the usual behavior of semiconductors for which the bandgap decreases as the temperature increases (negative  $dE_g/dT$ ), according to the empirical Varshni formula.<sup>[41]</sup> Although one might intuitively expect this decrease (redshift) as the lattice expands, in fact the lattice expansion is usually a relatively small contribution, and can increase or decrease the bandgap with temperature as determined by detailed band structure calculations.<sup>[42]</sup> The main contribution to the change in bandgap with temperature is the influence of phonons, i.e., the change in bandgap caused by the dynamic displacement of atoms due to thermal lattice vibrations (rather than the phonon anharmonicity responsible for lattice expansion).<sup>[43]</sup> Phonons usually reduce the bandgap as the temperature is raised, but can

increase it, and there can be multiple phonons with opposite effects on the bandgap in the same material, resulting in complex temperature dependence.<sup>[44]</sup> For metal halide perovskites it was initially proposed that the linear increase in bandgap with increasing temperature is due to the cancellation of phonon terms with opposite effect on the bandgap, leaving lattice expansion as the dominant contribution.<sup>[39]</sup> More recently, calculations have shown that the phonon anharmonicity is large, possibly making the lattice expansion explanation plausible without the need for other terms cancelling.<sup>[45]</sup> As the lattice constant is increased, the valence band maximum decreases linearly because of the reduced overlap of the Pb-6s and I-5s antibonding orbitals, therefore increasing the bandgap.<sup>[46]</sup> However another study has identified that the Pb-I-Pb bond bending phonon mode increases the bandgap and suggests this to be the main contribution.<sup>[47]</sup>

Figure 1d shows the gradient of the bandgap with respect to temperature in the highest and lowest temperature phase (as determined from linear fits to data shown in Figure S3, Supporting Information). In the room temperature phase, the bandgap of the 100% tin composition is the most sensitive to temperature (steepest gradient) and 100% lead the least, with the gradients of the mixed compositions linearly interpolating between the two. However, in the low temperature phase the gradient is smallest for the 65 and 85% Sn compositions. The phonon modes are thought to be relatively constant in the different phases of  $\text{FAPbI}_3$ ,<sup>[40]</sup> and our results show the temperature gradient is also the same in both phases measured. The tin-containing compositions all have different values of the temperature gradient for the two phases, which may indicate that the phonon modes are also different. It is also worth noting that the minimum gradient in the low temperature phase coincides with the minimum bandgap energy and seems to approximately follow the bowing in Figure 2a. If the main contribution to the temperature dependence of the bandgap is in fact lattice expansion, this could suggest hindered thermal expansion in the mixed compositions, possibly as a result of local strain to accommodate the different metal ions, which is also a factor that causes bandgap bowing.

## 2.2. Changes in Bandgap Bowing with Temperature

Given that both the structure and the temperature influence the bandgap, it is interesting to investigate how the bowing is affected. To determine the bandgap bowing parameter  $b$ , we fit Equation 1 to the absorption onset energy across the 6 compositions at a given temperature. Example fits are shown in Figure 2a for high and low temperature. We confirm that there is significant bandgap bowing, with the middle compositions having lower energy than the pure compositions, across all temperatures. Bandgap bowing has sometimes also been referred to as an “anomalous” bandgap, but we stress that it is simply the result of the generally applicable equation for semiconductor bandgaps (Equation 1), for a large value of  $b$ . Metal halide perovskites are essentially crystalline semiconductors, therefore we consider it informative for us to make a comparison with other materials that display bandgap bowing. For traditional inorganic semiconductors it is true that the

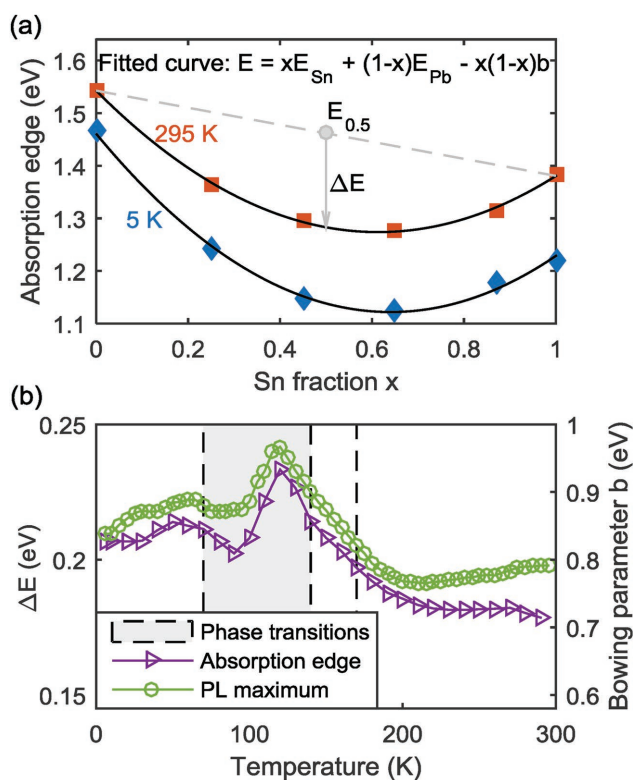


**Figure 2.** a) Absorption edge of  $\text{FAPb}_{1-x}\text{Sn}_x\text{I}_3$  at high (red squares) and low (blue diamonds) temperature. Black lines show fitted parabolas that determine the bowing parameter  $b$ . The dashed line shows the expected energies if the bandgap changed linearly, and  $\Delta E$  is the maximum deviation from linear (always at 50% Sn), which equals  $b/4$ . b) Bowing parameter calculated from fitting a parabola to the absorption edge energy (purple triangles), and the energy of maximum PL intensity (green circles) of all compositions, at each temperature. The shaded area shows the temperature region in which the phase transitions of the different compositions occur, and the dashed line at 170 K shows the extra phase transition of  $\text{FASnI}_3$ . For PL spectra, we excited the samples with a pulsed laser at 400 nm with a fluence of  $14 \text{ nJ cm}^{-2}$  and collected spectra at intervals of 5 K.

bowing parameter  $b$  is usually small compared to the size of the bandgap,<sup>[48]</sup> with only slight deviation from the linear behavior often referred to as “Vegard’s Law,”<sup>[49]</sup> which was however originally stated for lattice parameters rather than bandgaps. There are however a handful of semiconductors with bowing parameters large enough for the mixed compositions to have lower bandgaps than either of the end compositions, including  $\text{GaN}_x\text{As}_{1-x}$ ,  $\text{GaAs}_x\text{Sb}_{1-x}$ ,  $\text{CdSe}_x\text{Te}_{1-x}$  and  $\text{ZnS}_x\text{Te}_{1-x}$ .<sup>[48,50]</sup> Here, the bandgap bowing is thought to be caused by the local environment around the alloyed atom, meaning that averaging the properties of the alloy atoms (the “Virtual Crystal Approximation”) is not valid. Extended X-ray absorption fine structure measurements show that for pseudo-binary alloys such as those we have listed, the individual bond lengths are often closer to those of the un-alloyed materials, rather than adopting an intermediate value. The mismatch resulting from the different sizes of the alloyed atoms is then accommodated by local changes to bond angles, which results in properties that cannot be described by considering the global structure where the bond lengths take an average value and the angles are all

the same.<sup>[51,52]</sup> In perovskites the bond angles, specifically the tilting of the octahedra, have been shown to be important in determining the bandgap<sup>[20,53]</sup> and may provide a rationale for the large bowing parameter. These effects can be calculated using density functional theory (DFT), but since the local placement of the atoms is important, large supercells are required, making it computationally expensive to model. DFT has been used to calculate bowing in  $\text{FAPb}_{1-x}\text{Sn}_x\text{I}_3$  for a  $2 \times 2 \times 2$  supercell with some success despite the small size.<sup>[7]</sup> However, more in-depth calculations are required to allow for a full understanding of such effects in hybrid metal halide perovskites.

In certain cases (usually where the size or electronegativity of the alloy atoms differ greatly from each other) bandgap bowing can be described by considering an atom as an impurity that forms a new localized energy level which, if sufficiently close in energy, mixes with the conduction or valence band to form two new bands.<sup>[54]</sup> The bowing can then be modelled by a simple “band anticrossing” equation,<sup>[54]</sup> interpolated between the two impurity limits<sup>[55]</sup> and in some cases producing highly nonparabolic bowing.<sup>[56]</sup> We note however that our data are well represented by the parabolic model of bowing at all temperatures. It is therefore unlikely that the band anticrossing model of bowing is applicable here, since this characteristically results in highly nonparabolic bowing, with a sudden drop in bandgap at one end of the composition range, which we do not observe for the tin–lead perovskites at any composition or temperature.

To determine the effect of temperature on bandgap bowing, we extract the bowing parameter  $b$  from both PL and absorption data, as shown in Figure 2b as a function of temperature. In the shaded temperature region, individual compositions undergo phase transitions at different temperature, with the corresponding jump in bandgap leading to strong fluctuations of the extracted bowing parameter. However, outside of this intermediate range, we observe a roughly constant bowing parameter in both the low temperature region ( $\approx 0\text{--}70 \text{ K}$ ) and the high temperature region ( $\approx 170\text{--}300 \text{ K}$ ) within which no phase transitions occur. Absorption data indicate a bowing parameter of 0.73 eV for the high temperature phase and 0.84 eV for the low temperature phase (see also Figure S15, Supporting Information) highlighting the influence of crystal structure on the extent of bandgap bowing.

We note that the bowing calculated from PL measurements is higher than that calculated from the absorption onsets but the data converge at 5 K. These discrepancies can be understood by consideration of the changes in Stokes shift with temperature, shown in Figure S4 (Supporting Information). At room temperature, the PL peak energy will exhibit stronger bowing than at low temperature (5 K) because of the larger Stokes shift for the alloyed compositions. Similarly, it has been previously found for  $\text{InGaN}$  that PL measurements gave an overestimated bowing parameter, as a result of the larger Stokes shift of mixed compositions.<sup>[57]</sup> The absorption edge, as we have measured it, should be minimally affected by alloy disorder and therefore provides a more accurate value of the bandgap bowing parameter.

Overall, we conclude that bandgap bowing in tin–lead perovskites is likely to arise from bond bending to accommodate the random placement of lead and tin ions, given the parabolic nature of the large bowing we observe for all temperatures. The bowing parameter is largely constant with temperature for regions in which all compositions do not exhibit structural



phase transitions. However, crystal structure clearly has an effect on the magnitude of the bowing parameter, possibly through its influence on bond angles, suggesting that small structural changes, e.g., through A-cation choice, may be used to optimize desired bowing effects.

### 2.3. Changes in Emission Spectra with Tin–Lead Composition

We proceed by considering the influence of composition on disorder and PL quantum efficiency, which are highly important parameters for optimized power conversion efficiency of solar cells. For this purpose, we investigate the PL and absorption spectra at room temperature for 12 compositions with varying tin content (0%, 6.25%, 12.5%, 25%, 37.5%, 50%, 62.5%, 75%, 81.25%, 87.5%, 93.75%, and 100%).

#### 2.3.1. Spectral Broadening

The PL linewidth data (Figure 3a) show that the 100% tin and 100% lead iodide perovskites have much sharper PL spectra

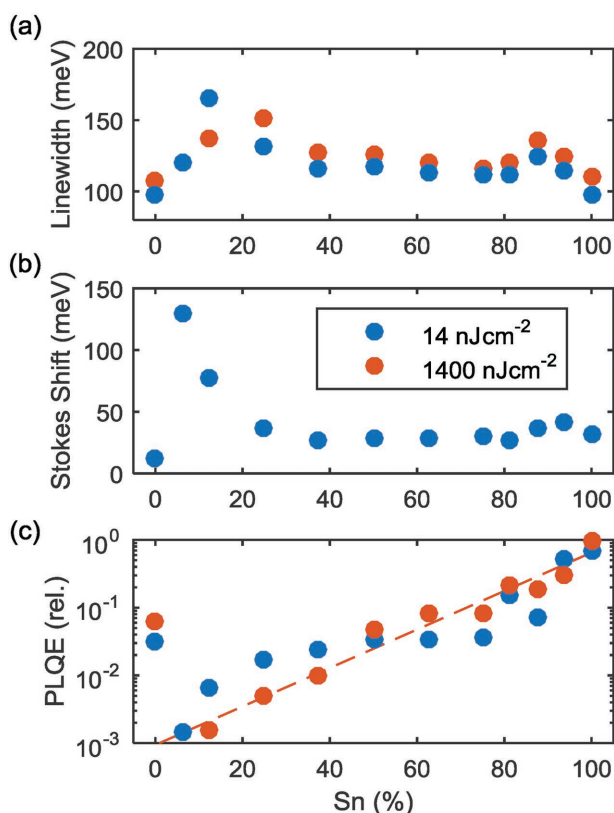


**Figure 3.** a) Full width at half maximum of the PL spectrum for each composition of  $\text{FAPb}_{1-x}\text{Sn}_x\text{I}_3$ , excited at 400 nm with a fluence of  $14 \text{ nJ cm}^{-2}$  (blue) and  $1400 \text{ nJ cm}^{-2}$  (red). b) Stokes shift of the same compositions determined by the difference between the absorption edge and the PL peak (400 nm,  $14 \text{ nJ cm}^{-2}$ ). c) Relative photoluminescence quantum efficiency (PLQE) for the same compositions, excited at 400 nm with a fluence of  $14 \text{ nJ cm}^{-2}$  (blue) and  $1400 \text{ nJ cm}^{-2}$  (red). The PLQE is normalized to the value for 100% Sn, measured at  $1400 \text{ nJ cm}^{-2}$  fluence. The dashed line shows an exponential fit to the high fluence data, excluding the 0% Sn point.

than those of their alloys, indicating higher disorder for mixed metal compositions. This observation is in agreement with the model discussed above, which assumes that random placement of tin and lead atoms on metal sites in the perovskite lattice is the main cause of bandgap bowing effects. From intuition and previous DFT calculations,<sup>[7]</sup> we would expect the linewidth to be broadest for the 50% composition, whereas in fact we find the broadest linewidth in the mixed compositions with Sn <25% and >85%. Since many material quality factors affect material disorder, this effect is likely to arise from extrinsic factors that can be improved with further crystal growth optimization, such as ensuring there are no inclusions of the yellow  $\delta$ -phase in the lead-rich compositions.<sup>[7,58]</sup> Interestingly the PL linewidth of  $\text{FASnI}_3$  is similar to that of  $\text{FAPbI}_3$ , and much narrower than that observed previously for  $\text{MASnI}_3$ ,<sup>[26]</sup> suggesting that  $\text{FASnI}_3$  (as prepared here with excess  $\text{SnF}_2$ ) may be less disordered and therefore able to support higher device efficiencies than its MA equivalent.

#### 2.3.2. Stokes Shift

The Stokes shift between emission peak and absorption edge is found to rise steeply when tin is added, then drops again and stays approximately constant for 40–100% tin content (Figure 3b). The large Stokes shift for materials with 6–12% Sn content suggests that a significant fraction of the PL originates from subbandgap states that exist in a severely disordered or defected material. Potential explanations could be a realignment of the level of trap states with respect to band edges as a small quantity of tin is added, or a structural instability (e.g., deterioration into a  $\delta$ -phase) causing an energetically disordered landscape. Particle size effects can also contribute to a change in Stokes shift for crystal sizes on the order of 10 nm and below,<sup>[59]</sup> but since the thickness and grain size for our films are in the 100–500 nm range,<sup>[7]</sup> we do not expect to see this effect.

#### 2.3.3. Quantum Efficiency

The PL quantum efficiency (PLQE) is of particular interest for solar cell applications because the presence of nonradiative recombination in the semiconductor implies there will be detrimental recombination in the photovoltaic device; therefore a higher PLQE of an absorber material will generally allow for higher PCEs. Here we examine relative PLQE values by dividing the luminescence intensity by the excitation power, across the tin–lead composition range. Figure 3c shows that the relative PLQE drops by almost 2 orders of magnitude when only 6% tin is added to  $\text{FAPbI}_3$ , but then rises exponentially as the tin content is increased. The sudden drop in PLQE for small additions of tin may have similar causes to those leading to the large Stokes shift for these compositions, e.g., an unfavorable re-alignment of trap levels or increase in their density, or an increase in energetic disorder. As we show in Section 2.4.1, the subsequent rise in PLQE with increasing tin content above 50% can be mainly understood in the context of an increased density of background holes present caused by spontaneous doping,

which has been associated with the propensity of the material to form Sn vacancies.<sup>[28,60]</sup> As a result, FASnI<sub>3</sub> has the highest PLQE in the series, being 10 times brighter than FAPbI<sub>3</sub>.

#### 2.4. Charge-Carrier Recombination Dynamics

Charge-carrier recombination processes compete with charge extraction in working solar cells. To investigate how such mechanisms are affected by composition in mixed-lead iodide perovskites, we acquired PL transients for a range of different temperatures and excitation fluences. The following rate equation is often used in the literature<sup>[1,27,61–63]</sup> to describe the time-dependence of a photogenerated charge-carrier density  $\Delta n$

$$\begin{aligned} \frac{d(\Delta n)}{dt} &= -k_1^{nr} \Delta n - k_2^r (p_0 + \Delta n) \cdot \Delta n \\ &= -(k_1^{nr} + k_1^r) \Delta n - k_2^r \Delta n^2 \end{aligned} \quad (2)$$

Here,  $k_1^{nr}$  is the monomolecular nonradiative recombination rate that typically reflects trap-mediated Shockley–Read–Hall recombination,  $k_2^r$  is the bimolecular radiative recombination rate constant, and  $p_0$  is the extrinsic background hole density present in the dark as a result of doping. Previous studies have shown significant contributions from a monomolecular radiative rate  $k_1^r = p_0 k_2^r$ , attributed to the recombination of photogenerated electrons with holes arising from doping.<sup>[61]</sup> Equation 2 inherently captures the dependence of the measured decay transients on the fluence of the initial excitation pulse. For low fluences, a monoexponential decay with time constant  $(k_1^{nr} + k_1^r)^{-1}$  is expected, while at higher fluences, bi-molecular decay kinetics lead to accelerated, non-exponential dynamics. However, as we argue below, Shockley–Read–Hall recombination does not necessarily always lead to monoexponential decay dynamics even in the low fluence regime, either because of a spatially uneven trap distribution, or the nature of the trap levels. We therefore choose instead to parameterize the decay curves with a stretched exponential  $I = I_0 \exp[-(t/\tau)^\beta]$  and extract  $\tau_{\text{eff}}$ , the effective lifetime and  $\beta$ , the stretch parameter.

##### 2.4.1. PL Transients as a Function of Tin–Lead Composition

Figure 4 demonstrates that the charge-carrier recombination kinetics fall into two distinct compositional regions: a lead rich region with Sn < 50% that exhibits stretched decay curves ( $\beta < 1$ ) and longer lifetimes, and a tin rich region with monoexponential decay curves ( $\beta = 1$ ) and short lifetimes. Since the tin rich compositions have reduced lifetimes, we can conclude that their higher PLQE is caused by a relative increase in radiative recombination rate, rather than a decrease in nonradiative recombination rate. A survey of the literature values reveals that the apparent radiative bimolecular recombination constant  $k_2$  is twice as large for FASnI<sub>3</sub><sup>[61]</sup> than FAPbI<sub>3</sub>,<sup>[64]</sup> with an intermediate value for a composition with 50% Sn.<sup>[7]</sup> Therefore, an enhancement in radiative recombination for tin-rich samples could be partly accounted for by enhanced band-to-band

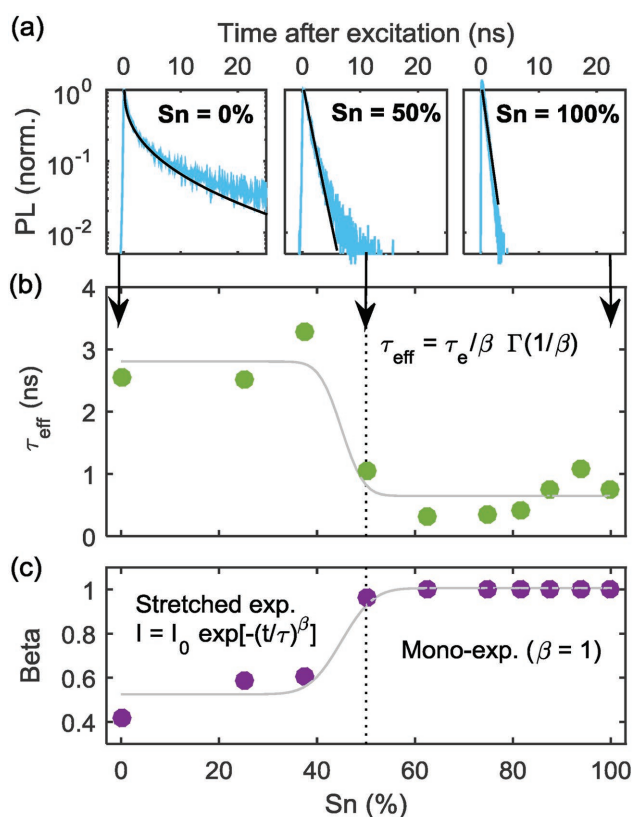


**Figure 4.** a) Example PL decay curves (blue) of FAPb<sub>1-x</sub>Sn<sub>x</sub>I<sub>3</sub> compositions at room temperature when excited at 400 nm with a fluence of 14 nJ cm<sup>-2</sup>, fitted (black) with a stretched exponential ( $I = I_0 \exp[-(t/\tau)^\beta]$ ), where beta is the stretch parameter. PL decay curves for other compositions are shown in Figure S6 (Supporting Information). From these fits, (b) shows the PL effective lifetime ( $\tau_{\text{eff}} = \tau_e / \beta \Gamma(1/\beta)$ ) where  $\Gamma$  is the gamma function) and c) the stretch parameter. Perovskites containing only 6.25% and 12.5% Sn were too weakly luminescent to be measured at this excitation intensity, but could be examined at a higher excitation intensity for which they also exhibit a long PL lifetime and stretched decay (Figure S7, Supporting Information).

recombination. However, such effects cannot fully account for the order of magnitude rise in PLQE between the lead and tin perovskites. We therefore attribute the increased luminescence of the tin-rich compositions to enhanced radiative recombination mediated by hole doping, an explanation which is consistent with Hall measurements<sup>[65,66]</sup> and other techniques<sup>[27,61]</sup> that have reported high doping densities for various tin-based perovskites, although such effects may be reduced substantially through suitable processing methods.<sup>[37,38]</sup>

In addition, analysis of the stretch-parameter  $\beta$  (Figure 4c) can yield interesting insights into the mechanisms for charge recombination. As we show below, the nonradiative recombination rate for a fluence of 14 nJ cm<sup>-2</sup> exceeds the radiative rate by at least a factor 100 across all compositions at room temperature and hence it is the trap-mediated recombination that will determine the dynamics. The nonradiative recombination of charge-carriers in semiconductors is generally described by the SRH model.<sup>[67]</sup> For many cases, the common assumption of a constant decay rate  $k_1$  (as in Equation 2) is a good approximation to SRH recombination, applicable to many situations such as extrinsically doped semiconductors, and leads

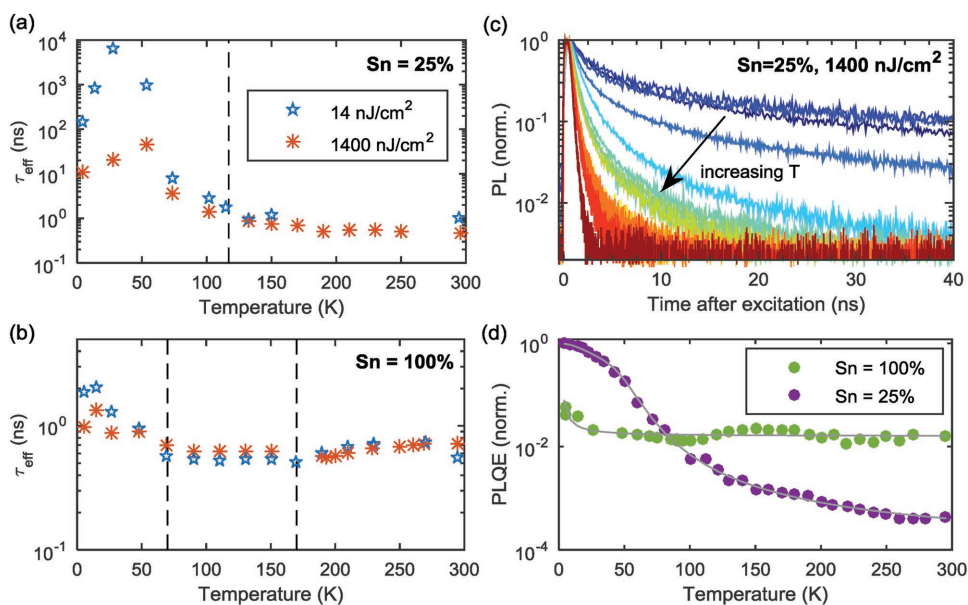


**Figure 5.** a,b) Effective PL lifetime determined from stretched exponential fits to PL transients for  $\text{FASn}_x\text{Pb}_{1-x}\text{I}_3$  with  $x = 0.25$  and  $1$ ; samples were excited at  $400\text{ nm}$  with a fluence of  $14$  and  $1400\text{ nJ cm}^{-2}$ . Phase transitions are shown by black dashed lines. c) Temperature-dependent PL decay curves for the  $x = 0.25$  sample excited at  $400\text{ nm}$  with a pulse energy of  $1400\text{ nJ cm}^{-2}$ . d) Relative PL intensity for  $x = 0.25$  and  $x = 1$  when samples were excited at  $400\text{ nm}$  with a power of  $1\text{ W cm}^{-2}$  pulsed at  $80\text{ MHz}$ . PLQE for  $x = 1$  is fixed relative to  $x = 0.25$  at  $295\text{ K}$  from Figure S4a (Supporting Information). The PLQE is normalized by setting the intensity of the  $25\%$  Sn composition at  $T = 5\text{ K}$  to a PLQE of  $1$  and scaling all other data by the same factor. Gray lines are fits, shown here as guides to the eye and discussed in the Supporting Information.

to monoexponential decay dynamics. However the full SRH formula has a more complex dependence on the photoexcited carrier density  $\Delta n$  that can result in nonexponential charge-carrier decay, e.g., for the case of intrinsic semiconductors with shallow traps (see Equation S7 and discussion in the Supporting Information). Nonexponential PL decay is also possible when the PL dynamics are determined by trap-filling rather than trap-assisted recombination (see Section S3.3, Supporting Information).<sup>[68,69]</sup> For lead triiodide perovskites, theoretical calculations have previously found the typical defect states to be very shallow<sup>[70]</sup> and the doping level to be intrinsic,<sup>[71]</sup> which is consistent with the stretched-exponential behavior we observe for the lead-rich compositions. Hence the transition to monoexponential decays for tin-rich compositions could be caused either by the substantial increase in doping density that we have already proposed, or by an increase in trap depth.

Overall, our observation of two distinct regimes for the stretch-parameter  $\beta$  suggests that there is a substantial change in the nature of defect formation at around  $50\%$  Sn. Based on the enhanced PLQE and shorter lifetimes for high tin content, this change is likely to cause or be accompanied by a change in doping density. A recent study investigating the stability of  $\text{FAPb}_{1-x}\text{Sn}_x\text{I}_3$  showed that compositions with less than  $50\%$  Sn were far more air-stable than tin-rich compositions, as a result of two different degradation mechanisms dominating in the two different regimes.<sup>[72]</sup> Although we did not intentionally expose our samples to air during either fabrication or measurement, spontaneous defect formation would follow similar thermodynamic considerations. Hence a switch in the nature of the defects between tin rich ( $x > 0.5$ ) and lead rich perovskites ( $x < 0.5$ ) is also the most likely explanation for the change in the shape of the decay transients we observe here.

#### 2.4.2. PL Transients as a Function of Temperature

To allow for an identification of trap-mediated charge-carrier recombination mechanisms, we investigate the temperature dependence of the PL dynamics. PL transients (Figure 5c, and Figures S8 and S9 in the Supporting Information) were measured for three compositions ( $25\%$ ,  $87.5\%$ , and  $100\%$  Sn) at temperatures between  $5$  and  $295\text{ K}$  for low and high fluences of  $14\text{ nJ cm}^{-2}$  and  $1400\text{ nJ cm}^{-2}$ . Figure 5a,b shows example values of the extracted effective PL lifetimes as a function of temperature for the  $25\%$  and  $100\%$  Sn perovskites, with further data shown in Figure S10 (Supporting Information).

We find that the effective PL lifetime increases with decreasing temperature for all compositions investigated, but more so for the tin-poor samples than for the  $100\%$  Sn perovskite whose PL lifetimes show only weak dependence on temperature. To investigate whether such effects are the result of changes in radiative or nonradiative decay pathways, we also recorded the relative PL quantum efficiencies as a function of temperature, shown in Figure 5d. The observed strong increase in relative PLQE for the  $25\%$  Sn perovskite with decreasing temperature indicates that the concomitant increase in PL lifetime is mostly related to a decrease in the nonradiative (trap-mediated) recombination rate ( $k_1^{nr}$  in Equation 2). Similar observations have previously been made for  $\text{MAPbI}_3$  for which  $k_1$  was shown to decrease upon cooling,<sup>[31]</sup> and for  $\text{FAPbI}_3$  where the PLQE was shown to have a similarly strong temperature dependence.<sup>[32]</sup>

We note that higher radiative efficiencies at lower temperature may also result from an increase in the radiative bimolecular recombination rate constant  $k_2$  with decreasing temperature. Such trends would be expected, as such band-to-band

recombination has recently been shown to be the inverse process to absorption (by the principle of detailed balance) and therefore the enhancement at low temperature is caused by the sharpening of the photon and charge carrier distribution functions.<sup>[2]</sup> We do indeed find that the PL lifetimes reduce ( $k_2$  higher) at low temperature (<60 K), where such radiative band-to-band recombination begins to play a larger role, evidenced by the higher PLQE. The difference in PL lifetimes for high and low excitation in this temperature region also supports the larger role of  $k_2$ . However, if it were the dominant process across all temperatures at the excitation fluences used, we would expect PL lifetimes to decrease with decreasing temperature, which is not observed. We therefore conclude, in agreement with our arguments above, that nonradiative trap-mediated processes are the primary cause of the increased PL lifetime and PLQE as temperature is decreased, and dominate the charge-carrier recombination processes at room temperature here.

To understand the temperature dependence of these trap-mediated charge-carrier recombination processes we consider several mechanisms within the theory of Shockley–Read–Hall recombination. The rate of SRH recombination (or alternatively of trap filling, see Section S3.3, Supporting Information) depends on charge carrier densities and on the lifetimes of the trapped electrons and holes (see Section S3.2 in the Supporting Information for a detailed discussion). The temperature dependence of the charge-carrier densities can be calculated from the Fermi–Dirac statistics—the densities reduce as the temperature is lowered. The SRH lifetimes, corresponding to the rates at which electrons and holes are trapped, are determined by the physical mechanism of recombination and can therefore display a variety of temperature-dependent behaviors. For clarity we will discuss the mechanisms in terms of electron trapping, but the mechanisms are equivalent for hole trapping. The most common mechanism in traditional semiconductors is multiphonon recombination, during which a trapped electron moves to a lower energy level by converting its energy into several phonons.<sup>[73]</sup> There is an activation energy associated with this process because energy and momentum conservation requires a number of particular phonons to be absorbed, in addition to those emitted.<sup>[74]</sup> The temperature dependence of the process depends on conditions such as the charge of the trap, whether the transition is between localized states or bands, and the possibility for quantum tunneling through the energy barrier, but in all cases the rate is expected to increase with temperature according to a power law or exponential rise, which has indeed been observed in experiments.<sup>[75]</sup> An alternative mechanism is cascade capture, where a charged trap has hydrogen-like excited states that an electron can cascade through by emitting a single phonon each time.<sup>[76]</sup> In contrast to the multiphonon process, the rate decreases with increasing temperature, since the electron is more likely to be thermally excited out of the first level.<sup>[75,76]</sup> The recombination rate is also expected to decrease in the presence of a continuous distribution of traps for the same reason.<sup>[77,78]</sup> As another channel (though one not included in the simple SRH model), trap-assisted Auger recombination may operate, during which an electron loses its energy to another electron.<sup>[79]</sup> Trap-assisted Auger recombination is only weakly dependent on temperature.<sup>[79]</sup> Finally, an electron can emit a photon when

it is captured, which would contribute to the PL spectrum at an energy lower than the bandgap. This process is also weakly dependent on temperature, but tends to be slower than the other mechanisms.<sup>[75]</sup>

With this knowledge of trap-mediated recombination processes in mind, we therefore conclude that the strongly temperature-activated nonradiative recombination channels in the 25% perovskite are most likely the result of multiphonon assisted SRH recombination. Fits to the relative PLQE yield an upper limit to the activation energy of around 40 meV for this process (see Section S2.2 in the Supporting Information for details). However to obtain a better fit at low temperature, an additional term must be included, which may be due either to the temperature dependence of radiative recombination<sup>[2]</sup> or to the presence of a distribution of traps, which is only distinguishable at low temperature, as proposed recently for FAPbI<sub>3</sub>.<sup>[78]</sup> However, we note that such fits also have an uncertainty because they do not take photon reabsorption into account.<sup>[80]</sup>

As Figure 5b,d illustrates, the 100% tin composition exhibits significantly less temperature-activated behavior, with PL lifetimes and relative PLQE only rising slightly with decreasing temperature. These data therefore suggest that, in FASnI<sub>3</sub>, either trap-assisted Auger recombination or multiphonon SRH recombination with a very small activation energy (0.5 meV from the fit in Figure 5d) is the predominant mechanism in operation. These are both nonradiative processes, accounting for the low relative PLQE. However, as discussed above, the SRH model predicts a trap-mediated monoexponential decay ( $\beta = 1$ ) of charge-carrier densities in the presence of high doping levels, whereas trap-assisted Auger recombination does not,<sup>[79]</sup> making an SRH mechanism the most likely nonradiative recombination process to be in action for FASnI<sub>3</sub> here. In contrast to what is observed for the 25% Sn composition, the PL lifetimes at high and low fluence are very similar at room temperature, and only show a small difference at low temperature. This is unsurprising given the large value of  $k_1$  indicated by the rapid monoexponential decay, meaning a very high fluence (much higher than the maximum of 1400 nJ cm<sup>-2</sup> used here) is needed to reach the carrier densities required to observe significant bimolecular recombination. We note also that for all compositions, we do not see any direct evidence of trap saturation, which could result in an increase in lifetime at higher fluence.

To summarize our findings for the charge-carrier recombination channels in FAPb<sub>1-x</sub>Sn<sub>x</sub>I<sub>3</sub>, we have shown that nonradiative pathways dominate for all compositions at room temperature at a fluence of 14 nJ cm<sup>-2</sup>. The lead-rich composition with 25% Sn has a temperature-activated nonradiative recombination pathway indicative of multiphonon recombination. In contrast, charge recombination channels in FASnI<sub>3</sub> (100% Sn) are hardly affected by temperature. We find that at room temperature the PL decay dynamics fall into a lead-rich regime with longer lifetimes and stretched exponential decays, and a tin-rich regime with shorter lifetimes and monoexponential decays. These observations are in agreement with a previous study showing that decomposition pathways, and hence defect formation, differ substantially in the tin- and lead-rich composition regimes.<sup>[72]</sup> We discussed that Shockley–Read–Hall statistics predict fluence-dependent charge-carrier recombination for intrinsic semiconductors, but fluence-independent



monoexponential behavior for heavily doped semiconductors, which underpins the difference in recombination dynamics we observe for these two regimes. Doping also enhances radiative recombination which, even if it is not the dominant mechanism in recombination dynamics, still increases the PLQE by an order of magnitude for FASnI<sub>3</sub> in comparison to FAPbI<sub>3</sub>.

### 3. Conclusion

In conclusion, we have demonstrated the important influence of composition and temperature on the bandgap and recombination mechanisms of FAPb<sub>1-x</sub>Sn<sub>x</sub>I<sub>3</sub>, two essential properties in the design of efficient solar cells. We have reported structural phase transition temperatures for mixed compositions for the first time and a bandgap bowing parameter of 0.73 and 0.84 eV for the room temperature and low temperature phases respectively, showing that crystal structure influences the magnitude of bowing. We have used a combination of temperature-dependent transient PL and PLQE measurements to distinguish different recombination mechanisms, showing that there is still considerable nonradiative recombination at room temperature in both 25% and 100% Sn compositions. This strongly suggests that efforts to increase charge-carrier lifetimes of tin-rich perovskites should focus not only on controlling doping densities but also on reducing nonradiative recombination via trap states. For our range of compositions of FAPb<sub>1-x</sub>Sn<sub>x</sub>I<sub>3</sub> we find the perovskite with around 40% Sn to be the most promising low bandgap material for use in tandem solar cells. FAPb<sub>0.6</sub>Sn<sub>0.4</sub>I<sub>3</sub> combines the long charge-carrier lifetime of the lead-rich materials with a PLQE approaching that of FAPbI<sub>3</sub> and a relatively small Stokes shift and PL linewidth compared to the other alloys. Its bandgap of around 1.3 eV is suitable for tandem devices and fairly close to the minimum achievable for FAPb<sub>1-x</sub>Sn<sub>x</sub>I<sub>3</sub> alloys. However, our work highlights that the optoelectronic properties of these materials are still highly dominated by extrinsic effects. Therefore, more favorable properties may still be obtained across the series with additional materials engineering, such as the optimization of treatments with compounds such as SnF<sub>2</sub> to increase the charge-carrier lifetime of the tin-rich compositions or addition of other cations and halides to tune the structural properties, which will influence both the bandgap bowing and the charge-carrier lifetimes. Our study highlights the link between such structural and optoelectronic properties, thus paving a way toward more guided materials design.

### 4. Experimental Section

**Sample Preparation:** FAPb<sub>1-x</sub>Sn<sub>x</sub>I<sub>3</sub> perovskite thin films were formed on z-cut quartz disks by spin-coating precursor solutions of FASnI<sub>3</sub> and FAPbI<sub>3</sub> in appropriate ratios. The precursor solutions were prepared at a concentration of 1 M in a mixed solvent of DMF:DMSO 65:35 by volume. The solutions were dissolved at a 1:1 molar ratio of formamidinium iodide (HC(NH<sub>2</sub>)<sub>2</sub>I) to tin iodide (SnI<sub>2</sub>) or lead iodide (PbI<sub>2</sub>). In addition, excess SnF<sub>2</sub> (0.2 M) was added into the FASnI<sub>3</sub> precursor (i.e., providing a 20% excess of tin). The Sn and Pb containing solutions were then mixed in the appropriate ratio before spin-coating at 5000 rpm in a nitrogen-filled glovebox. After dropping the solution onto the spinning substrate the speed was ramped down to zero (≈5 s). The wet transparent film was

then immediately immersed into a small petri dish containing anisole (≈5s) and blow-dried with a nitrogen gun. Anisole was not used for the 45 and 65% Sn samples which were spin-coated for 12 s including a ramp up (≈6s), blow-dried with a nitrogen-gun while still spinning for 16 s, spin-coated for a further 8 s followed by a ramp down (≈5s) which obtained uniform film coverage. A comparison of the films made with and without anisole for 87.5% Sn is found in Figure S11 (Supporting Information). The reddish or transparent precursor films were then annealed at 70 °C for 20 min. For the pure Pb and 6.25% Sn films, annealing at 170 °C for 10 and 1 min respectively was necessary to form the black phase perovskite as it formed the yellow phase when heated only at 70 °C. Our tin-rich compositions degrade when exposed to air, turning visibly transparent within hours or days, which is a well known problem with tin halide perovskites (see also our previous results for samples fabricated in the same way<sup>[7]</sup>). For this reason, all samples were fabricated inside a nitrogen filled glovebox and mounted in a vacuum chamber or sealed cryostat while still inside the glovebox to eliminate exposure to air. The chamber/cryostat was then transferred to the laser laboratory and evacuated, maintaining a pressure below 10<sup>-5</sup> mbar during measurements. This was effective at preventing degradation, as shown, e.g., by our repeated measurements of a sample with 87.5% tin content, giving the same results when measured at the beginning and end of a 2 month time interval.

**Photoluminescence Spectra:** To control the temperature, the sample was mounted in a cold-finger cryostat (MicrostatHe, Oxford Instruments). The temperature was controlled by a flow of liquid helium and an electronic temperature controller (ITC503, Oxford Instruments). The temperature was monitored with sensors both on the cryostat heat exchanger and the end of the sample holder. Samples were excited with the aid of a tunable Ti:Sapphire pulsed (80 fs) laser, with its fundamental wavelength set to 800 nm and an 80 MHz repetition rate (Mai Tai, Spectra-Physics). A BBO crystal was used to double the excitation frequency, giving an excitation wavelength of 400 nm. The 800 nm fundamental wavelength was filtered out using a polarizer and a color filter. The excitation intensity was attenuated using an OD1 filter and a variable attenuator consisting of a waveplate and a vertical polarizer to achieve 1 or 100 mW over a beam size of 0.09 mm<sup>2</sup>, giving fluences of 14 or 1400 nJ cm<sup>-2</sup>, corresponding to charge carrier densities on the order of 10<sup>15</sup> and 10<sup>17</sup> respectively. A horizontal polarizer and a 550 nm long-pass color filter were placed after the sample to remove any laser scatter from the spectrum. Photoluminescence from the sample was collected by a pair of off-axis parabolic mirrors and focused onto the entry slit of a grating monochromator (Triax, Horiba). The spectrally resolved PL was detected by a nitrogen-cooled Si-CCD detector (Symphony, Horiba) and the spectral response of all components was corrected for using a tungsten filament lamp with known spectrum. This is particularly important for tin perovskites since the sensitivity of the CCD drops off in the NIR where these materials emit.

**Transient Photoluminescence:** The setup for time-resolved photoluminescence for the compositions with Sn>50% was the same as above, except that light emitted at the peak PL wavelength was selected by a second slit and detected by a silicon single photon avalanche diode used for time correlated single photon counting. The instrument response function was measured by tuning the (80 fs pulsed) laser to the wavelength of the luminescence for each sample (since the detector response is slightly dependent on detection wavelength), and measuring the response due to laser scatter from a roughened quartz disk placed in the sample holder. The excitation powers used were 1 and 100 mW over a beam size of 0.09 mm<sup>2</sup> pulsed at 80 MHz, giving fluences of 14 and 1400 nJ cm<sup>-2</sup>.

For the compositions with Sn ≤ 50%, the decay time was too long for the pulse window. Instead an electronically pulsed diode laser with variable pulse frequency (PicoHarp LDH-D-C-405M) was used for excitation, the wavelength was selected using Princeton Instruments SP-2558 grating spectrometer before detection by a silicon single photon avalanche diode. The excitation power was chosen to match the fluence (14 and 1400 nJ cm<sup>-2</sup>) over a beam size of 0.018 mm<sup>2</sup> for various pulse rates between 0.5 and 20 MHz.

**Optical Absorption:** Samples were mounted in a helium gas exchange cryostat to control the temperature, with the same set-up for temperature control as the PL measurements. However, due to the configuration of the system, the samples had to be exposed to air for about a minute during transfer before being measured under vacuum.

Visible to NIR transmission and reflection measurements were performed using a Fourier transform infrared spectrometer (Vertex 80v, Bruker). A tungsten halogen lamp was used as a light source, and the light passing through the sample (T) and reflected from the sample (R) was detected by a nitrogen cooled InSb detector (NIR) and a silicon diode detector (visible). A blank substrate and a silver mirror were used as references for 100% transmission and reflection respectively. Background measurements were also used to correct for any scatter from the sample holder and other optical components. The absorbance was calculated from the measured transmission and reflection (Equation S1, Supporting Information). The absorption edge was defined as the point on the absorption curve with the steepest gradient, and was found by differentiation of the curve in the region of the absorption onset. This definition will give a slightly larger energy than that determined by a Tauc Plot, but we prefer this method since the exciton enhancement of the band edge<sup>[81]</sup> makes the Tauc Plot reading unphysical, and may be part of the reason for the wide range of bandgap energies reported (see Section S2.1 in the Supporting Information for more details).

## Supporting Information

Supporting Information is available from the Wiley Online Library or from the author.

## Acknowledgements

The authors acknowledge the Engineering and Physical Sciences Research Council (EPSRC) and the EU Horizon 2020 Programme (INFORM ITN Grant No. 675867) for financial support. E.S.P. thanks the EPSRC Centre for Doctoral Training in New and Sustainable Photovoltaics (CDT-PV) for support through a doctoral studentship.

## Conflict of Interest

The authors declare no conflict of interest.

## Keywords

bandgap bowing, perovskite solar cells, photoluminescence, recombination

Received: April 24, 2018  
Revised: May 19, 2018  
Published online: June 21, 2018

- [1] L. M. Herz, *ACS Energy Lett.* **2017**, *2*, 1539.  
[2] C. L. Davies, M. R. Filip, J. B. Patel, T. W. Crothers, C. Verdi, A. D. Wright, R. L. Milot, F. Giustino, M. B. Johnston, L. M. Herz, *Nat. Commun.* **2018**, *9*, 293.  
[3] W. S. Yang, B.-W. Park, E. H. Jung, N. J. Jeon, Y. C. Kim, D. U. Lee, S. S. Shin, J. Seo, E. K. Kim, J. H. Noh, S. Il Seok, *Science* **2017**, *356*, 1376.  
[4] D. Zhao, Y. Yu, C. Wang, W. Liao, N. Shrestha, C. R. Grice, A. J. Cimaroli, L. Guan, R. J. Ellingson, K. Zhu, X. Zhao, R.-G. Xiong, Y. Yan, *Nat. Energy* **2017**, *2*, 17018.

- [5] A. Rajagopal, Z. Yang, S. B. Jo, I. L. Braly, P. W. Liang, H. W. Hillhouse, A. K. Y. Jen, *Adv. Mater.* **2017**, *29*, 1.  
[6] F. Hao, C. C. Stoumpos, R. P. H. H. Chang, M. G. Kanatzidis, *J. Am. Chem. Soc.* **2014**, *136*, 8094.  
[7] G. E. Eperon, T. Leijtens, K. A. Bush, R. Prasanna, T. Green, D. P. Wang, J. T.-W. Mcmeekin, G. Volonakis, R. L. Milot, R. May, A. Palmstrom, D. J. Slotcavage, R. A. Belisle, J. B. Patel, E. S. Parrott, R. J. Sutton, W. Ma, F. Moghadam, B. Conings, A. Babayigit, H. Boyen, S. Bent, F. Giustino, L. M. Herz, M. B. Johnston, M. D. McGehee, H. J. Snaith, *Science* **2016**, *364*, 861.  
[8] O. J. Weber, B. Charles, M. T. Weller, *J. Mater. Chem. A* **2016**, *4*, 15375.  
[9] R. Prasanna, A. Gold-Parker, T. Leijtens, B. Conings, A. Babayigit, H. G. Boyen, M. F. Toney, M. D. McGehee, *J. Am. Chem. Soc.* **2017**, *139*, 11117.  
[10] W. Rehman, D. P. McMeekin, J. B. Patel, R. L. Milot, M. B. Johnston, H. J. Snaith, L. M. Herz, *Energy Environ. Sci.* **2017**, *10*, 361.  
[11] G. Xing, N. Mathews, S. S. Lim, N. Yantara, X. Liu, D. Sabba, M. Grätzel, S. Mhaisalkar, T. C. Sum, *Nat. Mater.* **2014**, *13*, 476.  
[12] J. H. Noh, S. H. Im, J. H. Heo, T. N. Mandal, S. Il Seok, *Nano Lett.* **2013**, *13*, 1764.  
[13] G. E. Eperon, S. D. Stranks, C. Menelaou, M. B. Johnston, L. M. Herz, H. J. Snaith, *Energy Environ. Sci.* **2014**, *7*, 982.  
[14] R. J. Sutton, G. E. Eperon, L. Miranda, E. S. Parrott, B. A. Kamino, J. B. Patel, M. T. Hörantner, M. B. Johnston, A. A. Haghighirad, D. T. Moore, H. J. Snaith, *Adv. Energy Mater.* **2016**, 1502458.  
[15] A. De Vos, *J. Phys. D: Appl. Phys.* **1980**, *13*, 839.  
[16] M. T. Hörantner, T. Leijtens, M. E. Ziffer, G. E. Eperon, M. G. Christoforo, M. D. McGehee, H. J. Snaith, *ACS Energy Lett.* **2017**, *2*, 2506.  
[17] S. Essig, C. Allebé, T. Remo, J. F. Geisz, M. A. Steiner, K. Horowitz, L. Barraud, J. S. Ward, M. Schnabel, A. Descoeurdes, D. L. Young, M. Woodhouse, M. Despeisse, C. Ballif, A. Tamboli, *Nat. Energy* **2017**, *2*, 17144.  
[18] G. E. Eperon, M. T. Hörantner, H. J. Snaith, *Nat. Rev. Chem.* **2017**, *1*, 95.  
[19] J. A. Van Vechten, T. K. Bergstresser, *Phys. Rev. B* **1970**, *1*, 3351.  
[20] J. Im, C. C. Stoumpos, H. Jin, A. J. Freeman, M. G. Kanatzidis, *J. Phys. Chem. Lett.* **2015**, *6*, 3203.  
[21] B. Zhao, M. Abdi-Jalebi, M. Tabachnyk, H. Glass, V. S. Kamboj, W. A. Nie, J. Pearson, Y. Puttisong, K. C. Gödel, H. E. Beere, D. A. Ritchie, A. D. Mohite, S. E. Dutton, R. H. Friend, A. Sadhanala, *Adv. Mater.* **2016**, *29*, 1604744.  
[22] M. Anaya, J. P. Correa-Baena, G. Lozano, M. Saliba, P. Anguita, B. Roose, A. Abate, U. Steiner, M. Grätzel, M. E. Calvo, A. Hagfeldt, H. Míguez, *J. Mater. Chem. A* **2016**, *4*, 11214.  
[23] C. Liu, J. Fan, H. Li, C. Zhang, Y. Mai, *Sci. Rep.* **2016**, *6*, 35705.  
[24] Z. Yang, A. Rajagopal, C. Chueh, S. B. Jo, B. Liu, T. Zhao, A. K. Jen, *Adv. Mater.* **2016**, *28*, 8990.  
[25] C. C. Stoumpos, M. G. Kanatzidis, *Acc. Chem. Res.* **2015**, *48*, 2791.  
[26] E. S. Parrott, R. L. Milot, T. Stergiopoulos, H. J. Snaith, M. B. Johnston, L. M. Herz, *J. Phys. Chem. Lett.* **2016**, *7*, 1321.  
[27] N. K. Noel, S. D. Stranks, A. Abate, C. Wehrenfennig, S. Guarnera, A. Haghighirad, A. Sadhanala, G. E. Eperon, S. K. Pathak, M. B. Johnston, A. Petrozza, L. Herz, H. Snaith, *Energy Environ. Sci.* **2014**, *7*, 3061.  
[28] Y. Y. Takahashi, R. Obara, Z.-Z. Lin, Y. Y. Takahashi, T. Naito, T. Inabe, S. Ishibashi, K. Terakura, *Dalton Trans.* **2011**, *40*, 5563.  
[29] W. Liao, D. Zhao, Y. Yu, N. Shrestha, K. Ghimire, C. R. Grice, C. Wang, Y. Xiao, A. J. Cimaroli, R. J. Ellingson, N. J. Podraza, K. Zhu, R. G. Xiong, Y. Yan, *J. Am. Chem. Soc.* **2016**, *138*, 12360.  
[30] Z. Zhao, F. Gu, Y. Li, W. Sun, S. Ye, H. Rao, Z. Liu, Z. Bian, C. Huang, *Adv. Sci.* **2017**, 1700204.  
[31] R. L. Milot, G. E. Eperon, H. J. Snaith, M. B. Johnston, L. M. Herz, *Adv. Funct. Mater.* **2015**, *25*, 6218.  
[32] H. Fang, F. Wang, S. Adjokatse, N. Zhao, J. Even, M. A. Loi, *Light: Sci. Appl.* **2016**, *5*, e16056.

- [33] T. Chen, B. J. Foley, C. Park, C. M. Brown, L. W. Harriger, J. Lee, J. Ruff, M. Yoon, J. J. Choi, S.-H. Lee, *Sci. Adv.* **2016**, 2, e1601650.
- [34] D. B. Mitzi, K. Liang, J. *Solid State Chem.* **1997**, 381, 376.
- [35] E. C. Schueller, G. Laurita, D. H. Fabini, C. C. Stoumpos, M. G. Kanatzidis, R. Seshadri, *Inorg. Chem.* **2018**, 57, 695.
- [36] T. M. Koh, T. Krishnamoorthy, N. Yantara, C. Shi, W. L. Leong, P. P. Boix, A. C. Grimsdale, S. G. Mhaisalkar, N. Mathews, *J. Mater. Chem. A* **2015**, 3, 14996.
- [37] C. C. Stoumpos, C. D. Malliakas, M. G. Kanatzidis, *Inorg. Chem.* **2013**, 52, 9019.
- [38] Y. Dang, Y. Zhou, X. Liu, D. Ju, S. Xia, H. Xia, X. Tao, *Angew. Chem., Int. Ed.* **2016**, 55, 3447.
- [39] C. Yu, Z. Chen, J. Wang, W. Pfenninger, N. Vockic, J. T. Kenney, K. Shum, *J. Appl. Phys.* **2011**, 110, 63526.
- [40] A. D. Wright, C. Verdi, R. L. Milot, G. E. Eperon, M. A. Pérez-Osorio, H. J. Snaith, F. Giustino, M. B. Johnston, L. M. Herz, *Nat. Commun.* **2016**, 7, 11755.
- [41] Y. P. Varshni, *Physica* **1967**, 34, 149.
- [42] P. B. Allen, V. Heine, *J. Phys. C: Solid State Phys.* **1976**, 9, 2305.
- [43] H. Y. Fan, *Phys. Rev.* **1951**, 82, 900.
- [44] A. Göbel, T. Ruf, M. Cardona, C. T. Lin, J. Wrzesinski, M. Steube, K. Reimann, J.-C. Merle, M. Joucla, *Phys. Rev. B* **1998**, 57, 15183.
- [45] L. D. Whalley, J. M. Skelton, J. M. Frost, A. Walsh, *Phys. Rev. B* **2016**, 94, 220301(R).
- [46] M. I. Dar, G. Jacopin, S. Meloni, A. Mattoni, N. Arora, A. Boziki, S. M. Zakeeruddin, U. Rothlisberger, M. Grätzel, *Sci. Adv.* **2016**, 2, e1601156.
- [47] H. Kim, J. Hunger, E. Cánovas, M. Karakus, Z. Mics, M. Grechko, D. Turchinovich, S. H. Parekh, M. Bonn, *Nat. Commun.* **2017**, 8, 687.
- [48] I. Vurgaftman, J. R. Meyer, L. R. Ram-Mohan, *J. Appl. Phys.* **2001**, 89, 5815.
- [49] L. Vegard, *Z. Phys.* **1921**, 5, 17.
- [50] I. Hernandez-Calderon, in *II-VI Semiconductor Materials and Their Applications* (Ed: M. C. Tamargo), Taylor & Francis, New York **2002**, pp. 113–170.
- [51] C. S. Schnohr, *Appl. Phys. Rev.* **2015**, 2, 31304.
- [52] J. B. Boyce, J. C. Mikkelsen, *J. Cryst. Growth* **1989**, 98, 37.
- [53] A. Amat, E. Mosconi, E. Ronca, C. Quarti, P. Umari, M. K. Nazeeruddin, M. Grätzel, F. De Angelis, *Nano Lett.* **2014**, 14, 3608.
- [54] W. Shan, W. Walukiewicz, J. Ager, E. Haller, J. Geisz, D. Friedman, J. Olson, S. Kurtz, *Phys. Rev. Lett.* **1999**, 82, 1221.
- [55] J. Wu, W. Shan, W. Walukiewicz, *Semicond. Sci. Technol.* **2002**, 17, 860.
- [56] K. M. Yu, S. V. Novikov, R. Broesler, A. X. Levander, Z. Liliental-Weber, F. Luckert, R. W. Martin, O. Dubon, J. Wu, W. Walukiewicz, C. T. Foxon, *Phys. Status Solidi C* **2011**, 8, 2503.
- [57] J. Wu, W. Walukiewicz, K. M. Yu, J. W. Ager, E. E. Haller, H. Lu, W. J. Schaff, *Appl. Phys. Lett.* **2002**, 80, 4741.
- [58] Z. Li, M. Yang, J. S. Park, S. H. Wei, J. J. Berry, K. Zhu, *Chem. Mater.* **2016**, 28, 284.
- [59] M. C. Brennan, J. Zinna, M. Kuno, *ACS Energy Lett.* **2017**, 2, 1487.
- [60] I. Chung, J. H. Song, J. Im, J. Androulakis, C. D. Malliakas, H. Li, A. J. Freeman, J. T. Kenney, M. G. Kanatzidis, *J. Am. Chem. Soc.* **2012**, 134, 8579.
- [61] R. L. Milot, G. E. Eperon, T. Green, H. J. Snaith, M. B. Johnston, L. M. Herz, *J. Phys. Chem. Lett.* **2016**, 7, 4178.
- [62] R. L. Milot, R. J. Sutton, G. E. Eperon, A. A. Haghighirad, J. Martinez Hardigree, L. Miranda, H. J. Snaith, M. B. Johnston, L. M. Herz, *Nano Lett.* **2016**, 16, 7001.
- [63] J. M. Richter, M. Abdi-Jalebi, A. Sadhanala, M. Tabachnyk, J. P. H. Rivett, L. M. Pazos-Outón, K. C. Gödel, M. Price, F. Deschler, R. H. Friend, *Nat. Commun.* **2016**, 7, 13941.
- [64] W. Rehman, R. L. Milot, G. E. Eperon, C. Wehrenfennig, J. L. Boland, H. J. Snaith, M. B. Johnston, L. M. Herz, *Adv. Mater.* **2015**, 27, 7938.
- [65] Y. Y. Takahashi, H. Hasegawa, Y. Y. Takahashi, T. Inabe, *J. Solid State Chem.* **2013**, 205, 39.
- [66] D. Sabba, H. K. Mulmudi, R. R. Prabhakar, T. Krishnamoorthy, T. Baikie, P. P. Boix, S. G. Mhaisalkar, N. Mathews, *J. Phys. Chem. C* **2015**, 119, 1763.
- [67] W. Shockley, W. T. Read, *Phys. Rev.* **1952**, 87, 835.
- [68] S. D. Stranks, V. M. Burlakov, T. Leijtens, J. M. Ball, A. Goriely, H. J. Snaith, *Phys. Rev. Appl.* **2014**, 2, 34007.
- [69] G. K. Wertheim, *Phys. Rev.* **1958**, 109, 1086.
- [70] J. Kim, S.-H. Lee, J. H. Lee, K.-H. Hong, *J. Phys. Chem. Lett.* **2014**, 5, 1312.
- [71] J. Huang, Y. Yuan, Y. Shao, Y. Yan, *Nat. Rev. Mater.* **2017**, 2, 17042.
- [72] T. Leijtens, R. Prasanna, A. Gold-Parker, M. F. Toney, M. D. McGehee, *ACS Energy Lett.* **2017**, 2, 2159.
- [73] R. N. Hall, *Proc. IEE – Part B: Electron. Commun. Eng.* **1959**, 106, 923.
- [74] A. Alkaskas, Q. Yan, C. G. Van De Walle, *Phys. Rev. B: Condens. Matter Mater. Phys.* **2014**, 90, 1.
- [75] V. L. Bonch-Bruевич, E. G. Landsberg, *Phys. Status Solidi* **1968**, 29, 9.
- [76] M. Lax, *J. Phys. Chem. Solids* **1959**, 8, 66.
- [77] D. Monroe, *Phys. Rev. Lett.* **1985**, 54, 146.
- [78] A. D. Wright, R. L. Milot, G. E. Eperon, H. J. Snaith, M. B. Johnston, L. M. Herz, *Adv. Funct. Mater.* **2017**, 27, 1700860.
- [79] D. J. Robbins, P. T. Landsberg, *J. Phys. C Solid State Phys.* **1980**, 13, 2425.
- [80] T. W. Crothers, R. L. Milot, J. B. Patel, E. S. Parrott, J. Schlipf, P. Müller-Buschbaum, M. B. Johnston, L. M. Herz, *Nano Lett.* **2017**, 17, 5782.
- [81] R. J. Elliott, *Phys. Rev.* **1957**, 108, 1384.
- [82] G. Kieslich, S. Sun, T. Cheetham, *Chem. Sci.* **2015**, 6, 3430.
- [83] S. G. Motti, M. Gandini, A. J. Barker, J. M. Ball, A. R. Srimath Kandada, A. Petrozza, *ACS Energy Lett.* **2016**, 1, 726.
- [84] T. Bin Song, T. Yokoyama, C. C. Stoumpos, J. Logsdon, D. H. Cao, M. R. Wasielewski, S. Aramaki, M. G. Kanatzidis, *J. Am. Chem. Soc.* **2017**, 139, 836.
- [85] M. A. Green, A. Ho-Baillie, H. J. Snaith, *Nat. Photonics* **2014**, 8, 506.
- [86] M. Leroux, N. Grandjean, B. Beaumont, G. Nataf, F. Semond, J. Massies, P. Gibart, *Phys. Status Solidi B* **1999**, 216, 605.
- [87] S. Sun, T. Salim, N. Mathews, M. Duchamp, C. Boothroyd, G. Xing, T. C. Sum, Y. M. Lam, *Energy Environ. Sci.* **2014**, 7, 399.
- [88] T. J. Savenije, C. S. Ponseca, L. Kuneman, M. Abdellah, K. Zheng, Y. Tian, Q. Zhu, S. E. Canton, I. G. Scheblykin, T. Pullerits, A. Yartsev, V. Sundstro, *J. Phys. Chem. Lett.* **2014**, 5, 2189.
- [89] K. Wu, A. Bera, C. Ma, Y. Du, Y. Yang, L. Li, T. Wu, *Phys. Chem. Chem. Phys.* **2014**, 16, 22476.
- [90] A. Miyata, A. Mitioglu, P. Plochocka, O. Portugall, J. T.-W. Wang, S. D. Stranks, H. J. Snaith, R. J. Nicholas, *Nat. Phys.* **2015**, 11, 582.
- [91] T. Leijtens, G. Eperon, A. Barker, G. Grancini, W. Zhang, J. Ball, A. R. Srimath Kandada, H. Snaith, A. Petrozza, *Energy Environ. Sci.* **2016**, 9, 3472.